Mean-field model of the von Kármán sodium dynamo experiment using soft iron impellers

C. Nore,[1,*] J. Léorat,[2] J.-L. Guermond,[1,3] and A. Giesecke[4]

[1]*Laboratoire d'Informatique pour la Mécanique et les Sciences de l'Ingénieur, CNRS UPR 3251, Rue John von Neumann, 91403 Orsay cedex, France and Université Paris-Sud, Paris, France*

[2]*Luth-Observatoire de Paris-Meudon, Place Janssen, 92195 Meudon, France*

[3]*Department of Mathematics, Texas A&M University, 3368 TAMU, College Station, Texas 77843-3368, USA*

[4]*Helmholtz-Zentrum Dresden-Rossendorf, P.O. Box 510119, D-01314 Dresden, Germany*

(Received 20 May 2014; revised manuscript received 16 October 2014; published 14 January 2015)

It has been observed that dynamo action occurs in the von-Kármán-Sodium (VKS) experiment only when the rotating disks and the blades are made of soft iron. The purpose of this paper is to numerically investigate the role of soft iron in the VKS dynamo scenario. This is done by using a mean-field model based on an axisymmetric mean flow, a localized permeability distribution, and a localized α effect modeling the action of the small velocity scales between the blades. The action of the rotating blades is modeled by an axisymmetric effective permeability field. Key properties of the flow giving to the numerical magnetic field a geometric structure similar to that observed experimentally are identified. Depending on the permeability of the disks and the effective permeability of the blades, the dynamo that is obtained is either oscillatory or stationary. Our numerical results confirm the leading role played by the ferromagnetic impellers. A scenario for the VKS dynamo is proposed.

DOI: 10.1103/PhysRevE.91.013008 PACS number(s): 47.65.−d, 52.65.Kj, 91.25.Cw

I. INTRODUCTION

Nearly a century after Larmor hypothesized that the solar magnetic field is the result of a magnetohydrodynamic (MHD) instability in the conducting plasma (*dynamo action*), the exact dynamical processes leading to MHD flows in astrophysical objects remain rather obscure. For instance, whether dynamo action can occur in a fully turbulent homogeneous flow without large scale structures remains an open question. After a considerable amount of observational, theoretical, and numerical evidence, the first successful experimental fluid dynamos were built in the early 2000s. At the present time, only three experiments have produced fluid dynamos. The first two experiments (Riga [1], Karlsruhe [2]) had a relatively low turbulence level and produced an equatorial dipolar magnetic field in agreement with the theoretical and numerical kinematic dynamo models assuming axisymmetric velocity fields. In contrast, the third one (von Kármán sodium experiment located in Cadarache [3], henceforth referred to as VKS) was highly turbulent and produced a magnetic field which was mainly axisymmetric and dipolar on average. It is reported in [4] that a necessary condition for dynamo action to occur in the VKS experiment is that at least one of the two counter-rotating impellers be made of soft iron. Moreover, this requirement applies to both the disks and the blades. More precisely, threshold estimates based on decay relaxation times and induction experiments show that adopting steel for one of these two elements moves the critical magnetic Reynolds number for dynamo action above 125[1] (using the definition of the magnetic Reynolds number from [4]), which is well above the largest value that can be reached in the experiment; see [4, Table I]. It thus appears instructive to examine the role of soft iron compared to steel: Is it that soft iron simply helps to lower the critical magnetic Reynolds number that can be reached in the VKS experiment, or does this material lead to a specific dynamo mechanism? The measurements in the VKS experiment cannot discriminate between the above two hypotheses. One important obstacle that prevents experimentalists to elucidate this dilemma is that the flow field in the liquid sodium cannot be observed, and even if it could (by replacing liquid sodium by water for instance) the flow between the blades is difficult to measure. This conundrum cannot be unequivocally resolved numerically either, yet, since simulating numerically the whole Cadarache experiment, including the rotating impellers, is not feasible with the numerical tools currently available. Some teams are working in this direction, though [5], including ours, and it is reasonable to think that numerical simulations of the VKS experiment at moderate kinetic and magnetic Reynolds numbers could be done in the near future.

The objective of the present paper is to propose a possible scenario for the VKS dynamo involving primarily the magnetic permeability of the impellers. We propose to investigate a kinematic dynamo model of the VKS experiment based on two simplifying assumptions about the blades: (i) the action of the small scales of the flow trapped between the blades is modeled by a localized α effect; (ii) the eight soft iron blades of the real impellers are modeled by using an axisymmetric distribution of effective relative magnetic permeability. The kinematic approach is certainly not capable of explaining all the details of the VKS experiment, but we posit that the essential characteristics of the VKS dynamo (critical magnetic Reynolds number around 30, axisymmetric geometry of the magnetic field, dynamo action only with soft iron impellers) can be captured by kinematic models close to the dynamo threshold. For instance, the kinematic approach gave satisfying descriptions of the dynamo process in the Karlsruhe and Riga experiments.

The paper is organized as follows. The problem under investigation and the numerical methods used to solve it are presented in Sec. II. Section III presents numerical

*Email address: caroline.nore@limsi.fr

[1]90 using the definition of the magnetic Reynolds number from [3].

TABLE I. Largest growth rates of the axisymmetric eigenmode with dipolar symmetry versus α, computed with SFEMANS and FV/BEM. OSC means that the frequency is nonzero.

α	γ (SFEMANS)	γ (FV/BEM)	OSC
−0.03	0.0127	0.0156	Yes
−0.015	−0.0167	−0.0155	Yes
−0.005	−0.0513	−0.0477	Yes
0	−0.0353	−0.0343	No
0.015	−0.0030	−0.0030	No
0.03	−0.0338	−0.0328	No
0.05	−0.0383	−0.0358	No

axisymmetric induction experiments that help to identify an expulsion mechanism that is detrimental to the dynamo effect. The range of parameters where dynamo action is achieved is examined in Sec. IV and some comparisons between the numerical model and the VKS experiment are attempted. It is shown in this section that it is possible to find a realistic range of values of α that triggers dynamo action provided the effective relative magnetic permeability in the region swept by the blades is large enough. It is also shown that in this range of values for α, the dynamo vanishes when the effective relative magnetic permeability of the impellers is that of steel. Concluding remarks are reported in Sec. V; key similarities between the VKS dynamo and our kinematic model are listed in Sec. V A and, finally, a tentative scenario for the VKS dynamo is proposed in Sec. V B.

II. PHYSICAL AND NUMERICAL SETTINGS

A. Geometry

We model the VKS device as a vessel composed of two concentric cylindrical containers closed at their extremities by two thin lids. (The exact configuration of the VKS experiment is described in [4,6].) The radius of the inner cylinder is henceforth defined to be the length unit, say $\mathcal{L}$. The nondimensional radius of the external cylinder is $R_e = 1.4$ and the nondimensional height of the vessel is $L = 2.6$. Using the cylindrical coordinates (r,θ,z), with the convention that the z axis is aligned with the axis of the cylindrical vessel, the computational domain, $0 \leqslant r \leqslant R_e$, $0 \leqslant \theta \leqslant 2\pi$, $|z| \leqslant L/2$, is denoted $\mathcal{D}$; see Fig. 1.

The vessel is assumed to be filled with liquid sodium, and the sodium enclosed between the inner and outer cylinders is kept stagnant at all times. The two impellers mounted at the extremities of the inner cylinder are each composed of a disk equipped with eight blades. The thickness and radial extension of the disks is 0.1 and 0.9, respectively; i.e., the region occupied by the disk is $0 \leqslant r \leqslant 0.9, 0 \leqslant \theta < 2\pi, 0.9 \leqslant |z| \leqslant 1$; see the shaded region labeled "Disk" in Fig. 1. The relative magnetic permeability of the disks is denoted μ_d. When rotating, the eight blades sweep a volume of height 0.2 and radius 0.9, i.e., the region occupied on average by the blades is $0 \leqslant r \leqslant 0.9$, $0 \leqslant \theta < 2\pi$, $0.7 \leqslant |z| \leqslant 0.9$; see the region with diagonal pattern labeled "Blades" in Fig. 1. The magnetic action of the blades is modeled by assigning an axisymmetric distribution of effective relative magnetic permeability to this volume, μ_b. The fluid enclosed between the two blade regions is free to move about in the inner cylinder. The vertical extension of this column of liquid sodium is denoted $2h$. Two sets of simulations will be done using either $h = 0.7$ or $h = 0.9$, as explained in Sec. III.

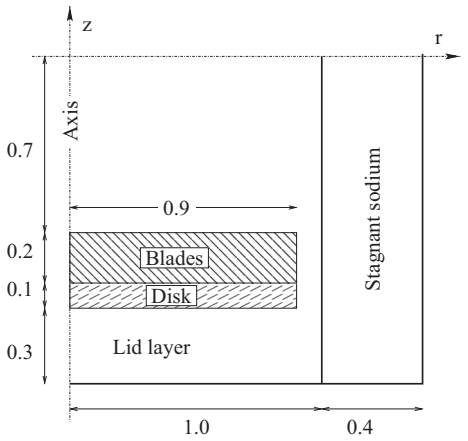

FIG. 1. Bottom half of the meridian section of the VKS numerical model.

B. Velocity field

Denoting by $\mathcal{U}$ the reference velocity, the nondimensional velocity field in the region $0 \leqslant r \leqslant 1, 0 \leqslant \theta < 2\pi, |z| \leqslant h$ is modeled by an analytical approximation of the averaged flow measured in a water model [7]:

$$\begin{aligned} u_r(r,z) &= -(\pi/2h)r(1-r)^2(1+2r)\cos(\pi z/h), \\ u_\theta(r,z) &= -4\epsilon r(1-r)\sin(\pi z/2h), \\ u_z(r,z) &= (1-r)(1+r-5r^2)\sin(\pi z/h), \end{aligned} \qquad \begin{cases} 0 \leqslant r \leqslant 1, \\ 0 \leqslant \theta < 2\pi, \\ |z| \leqslant h. \end{cases} \tag{2.1}$$

This vector field is henceforth called the MND flow in reference to the authors (Marié-Normand-Daviaud) of [7]. The parameter ϵ measures the ratio between the toroidal and poloidal components of the velocity field. We choose $\epsilon = 0.7259$ in the rest of the paper since this ratio has been shown in [8, Figs. 9, 10] to minimize the dynamo threshold. The maximum of the Euclidean norm of the field (2.1) is equal to 1; hence, the reference velocity $\mathcal{U}$ is equal to the maximum of the Euclidean norm of the velocity field. We discuss the cases $h = 0.7$ and $h = 0.9$ in Sec. III; the volume swept by the blades is not included in the MND flow in the first case but it is included in the second case. The velocity

in the volume $0 \leqslant r \leqslant 1, 0 \leqslant \theta < 2\pi, h \leqslant |z| \leqslant 1$, which is either the blade and disk region if $h = 0.7$ or only the disk region if $h = 0.9$, is assumed to be purely azimuthal and equal to the azimuthal component of the flow at $z = \pm h$; i.e., upon defining $\mathrm{sgn}(z) = z/|z|$, we set

$$\begin{aligned} u_r(r,z) &= 0, \\ u_\theta(r,z) &= -4\,\mathrm{sgn}(z)\epsilon r(1-r), \\ u_z(r,z) &= 0, \end{aligned} \qquad \begin{cases} 0 \leqslant r \leqslant 1, \\ 0 \leqslant \theta < 2\pi, \\ h \leqslant |z| \leqslant 1. \end{cases} \tag{2.2}$$

A lid-layer flow is also assumed to be established behind each impeller (i.e., in the domain $0 \leqslant r \leqslant 1, 0 \leqslant \theta < 2\pi, 1 \leqslant |z| \leqslant L/2$, see "Lid layer" in Fig. 1) and the corresponding velocity field is modeled by setting

$$\begin{aligned} u_r(r,z) &= 0, \\ u_\theta(r,z) &= -4\,\mathrm{sgn}(z)\epsilon r(1-r)(L-2|z|)/(L-2), \\ u_z(r,z) &= 0, \end{aligned} \qquad \begin{cases} 0 \leqslant r \leqslant 1, \\ 0 \leqslant \theta < 2\pi, \\ 1 \leqslant |z| \leqslant L/2. \end{cases} \tag{2.3}$$

The MND flow (2.1) is a reasonable divergence-free approximation of the mean axisymmetric velocity field measured in water experiments using the same driving mechanisms as in the VKS experiment [7,8]. The velocity fields (2.2) and (2.3) are simple analytical extensions of the MND flow that describe the rotation in the blade region and the decay of the velocity behind the impellers. It is shown in [9] that the way the flow is extended becomes less important when the magnetic permeability of the impeller disks is large.

C. The mean-field model

Since no measurement of the average flow between the blades is available, and the action of the blades is only accounted for in average, we must appropriately model the induction effect of the vortices that are trapped between the blades. We have chosen for this purpose to use the so-called *mean-field* dynamo theory; see, e.g., [10,11]. Denoting by $\mathbf{u}'$ the small scale flow and by $\mathbf{b}'$ the induced small scale magnetic induction, the mean-field approach consists of assuming that the mean electromotive force induced by the small scales of the velocity field is a linear function of the mean magnetic induction and its first derivative, i.e., $\langle \mathbf{u}' \times \mathbf{b}' \rangle_i = \mathbb{a}_{ij} B_j + \beta_{ijk} \partial_j B_k$, where the tensors $\mathbb{a}_{ij}$ and β_{ijk} are *a priori* anisotropic since the flow between the blades is strongly anisotropic. The simplest model for the β effect consists of setting $\beta_{ijk}\partial_j B_k \mathbf{e}_i = -\beta \nabla \times \mathbf{B}$, which just amounts to a change of electrical conductivity; see, e.g., [11, p. 194]. The α effect is the simplest mechanism that couples the poloidal and toroidal components of the magnetic field, which is the main requirement for a dynamo. In the following, in an effort to minimize the number of modeling parameters, we neglect the β effect and assume that $\mathbb{a}$ is diagonal. The components of the tensor $\mathbb{a}$ can be estimated by evaluating the interaction between the mean-field $\mathbf{B}$ and the jets trapped between the blades, which we assume to flow outward in the radial direction (see [5,12]). As explained in Fig. 2, applying an azimuthal or axial mean magnetic induction generates an electromotive force $\langle \mathbf{u}' \times \mathbf{b}' \rangle$ that is opposite to the applied mean field, and this electromotive force is zero on average if the mean field is radial. This heuristic arguments suggests that the dominant coefficients of the tensor $\mathbb{a}$ are $\mathbb{a}_{zz}$ and $\mathbb{a}_{\theta\theta}$ and these coefficients should be nonpositive.

We have performed a series of tests (data not shown) using either $\mathbb{a}_{zz} = \mathbb{a}_{\theta\theta} \neq 0$ or $\mathbb{a}_{zz} = 0$ with $\mathbb{a}_{\theta\theta} \neq 0$. These simulations have led us to conclude that using $\mathbb{a}_{zz} \neq 0$ does not significantly change the dynamo threshold. Hence, in an effort to reduce the number of free parameters, we set $\mathbb{a}_{zz} = 0$ in the rest of this paper and only keep $\mathbb{a}_{\theta\theta}$. The term $\mathbb{a}_{\theta\theta}(\mathbf{B}\cdot\mathbf{e}_\theta)\mathbf{e}_\theta$ is alone sufficient to close the dynamo loop; i.e., it converts toroidal energy into poloidal energy; see (2.6) . The coefficient $\mathbb{a}_{\theta\theta}$, henceforth denoted α, is additionally assumed to be uniform in the cylindrical volume swept by the blades ($0.7 \leqslant |z| \leqslant 0.9, r \leqslant 0.9$) and to be zero outside this domain; i.e., we restrict the action of the α effect to the blade region only. A realistic upper bound on α is the root-mean-square velocity of the turbulent fluctuations of the velocity in the impeller region. Since the characteristic velocity is of the same order as that of the impellers [see (2.1)–(2.3)], we consider that computational estimates of α are realistic provided they remain much smaller than the typical flow

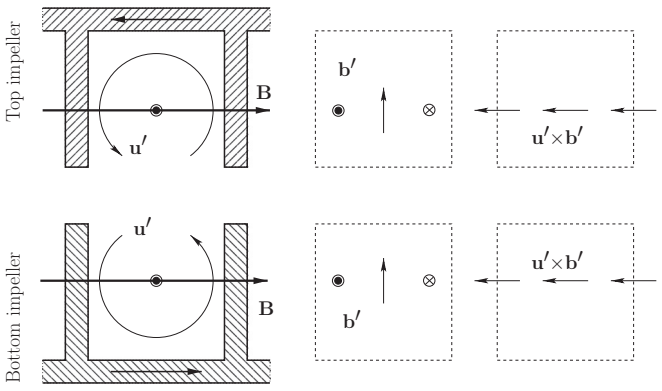

FIG. 2. Heuristics for the α model. The jet between the blades (top and bottom left) expels the fluid outward (thin arrow and outward symbol for $\mathbf{u}'$) and deforms the azimuthal component of the mean magnetic induction $\mathbf{B}$ (thick arrow), resulting in small scale perturbations $\mathbf{b}'$ (top and bottom center panels) which, in turn, generate an electromotive force $\mathbf{u}' \times \mathbf{b}'$ (top and bottom right). Note that $\mathbf{u}' \times \mathbf{b}'$ is opposite to $\mathbf{B}$. The same argument holds for a vertical mean magnetic induction. This argument shows also that the radial component of $\mathbf{B}$ yields an electromotive force that is zero on average, thereby implying that $\mathbb{a}_{rr}$ can be neglected.

speed; i.e., reasonable values of α should be in the range of a few percent of the typical flow speed. The above model is coherent with the Reynolds-averaged Navier–Stokes equations (RANS) simulations done in [13] on the VKS configuration. Using the Computational Fluid Dynamics finite-volume solver code FLUENT6.3 together with a $k-\epsilon$ RANS model, it is observed therein "that the helicity is mainly concentrated in the impellers" and, assuming that $\mathbb{a}$ is proportional to the helicity tensor, it is also observed that "the largest component of the tensor in the rotating impeller is $\mathbb{a}_{\theta\theta}$" and that it is negative. This is further substantiated by direct measurements of α in a toroidal screw flow leading to an estimate for α in liquid sodium of the order of $10^{-3},\dots,10^{-2}$ of the mean flow [14].

Recalling that the characteristic length $\mathcal{L}$ is the radius of the inner vessel and the characteristic velocity $\mathcal{U}$ is the maximum amplitude of the MND flow, we define the advection time $\mathcal{T}=\frac{\mathcal{L}}{\mathcal{U}}$ and introduce the magnetic Reynolds number $R_{\rm m}=\sigma_0\mu_0\mathcal{L}\mathcal{U}$. The parameters σ_0 and μ_0 are the electrical conductivity of liquid sodium and the magnetic permeability of the vacuum, respectively. Our definition of the magnetic Reynolds number is the same as in [3], assuming that the maximum velocity in the bulk of the flow is about 60% of the velocity at the rim of the blades; the 60% factor is the impeller efficiency estimated in [3]. Our magnetic Reynolds number is about 1.4 times smaller than that used in [4]. Using the above length, velocity, and time scales, the nondimensional mean field equation is

$$\begin{aligned}\partial_t\mathbf{B}=&\,\boldsymbol{\nabla}\times[(\mathbf{u}\times\mathbf{B})+\alpha(\mathbf{B}\cdot\mathbf{e}_\theta)\mathbf{e}_\theta]\\&-\frac{1}{R_{\rm m}}\boldsymbol{\nabla}\times\left[\frac{1}{\sigma_r}\boldsymbol{\nabla}\times\left(\frac{\mathbf{B}}{\mu_r}\right)\right],\end{aligned}\tag{2.4}$$

where σ_r and μ_r are the relative electrical conductivity and magnetic permeability fields, respectively; these parameters are not constant since the impellers may be composed of copper, steel, or soft iron. Since we have shown in [9, Fig. 7] that the magnetic permeability is the key material property that controls the ability of the impellers to store toroidal magnetic energy in the impellers, we assume in the rest of the paper that the conductivity is constant everywhere ($\sigma_r=1$) in order to minimize the number of free parameters. The relative permeability in the disks is chosen to be $\mu_d=60$, which is a value close to that measured in [15] for the soft iron impellers used in the VKS experiment. The permeability in the axisymmetric domain swept by the blades ($0.7\leqslant|z|\leqslant 0.9$, $r\leqslant 0.9$) is modeled by a uniform, effective, relative permeability in the range $1<\mu_b<\mu_d$ to take into account the partial filling of the volume by the blades. Note that owing to the identity $\boldsymbol{\nabla}\times(\mathbf{u}\times\mathbf{B})=\mathbf{B}\cdot\boldsymbol{\nabla}\mathbf{u}-\mathbf{u}\cdot\boldsymbol{\nabla}\mathbf{B}$, (2.4) can also be rewritten

$$\begin{aligned}&\frac{d\mathbf{B}}{dt}+\frac{1}{R_{\rm m}}\boldsymbol{\nabla}\times\left[\frac{1}{\sigma_r}\boldsymbol{\nabla}\times\left(\frac{\mathbf{B}}{\mu_r}\right)\right]\\&\quad=\mathbf{B}\cdot\boldsymbol{\nabla}\mathbf{u}+\boldsymbol{\nabla}\times[\alpha(\mathbf{B}\cdot\mathbf{e}_\theta)\mathbf{e}_\theta],\end{aligned}\tag{2.5}$$

where $\frac{d\mathbf{B}}{dt}:=\partial_t\mathbf{B}+\mathbf{u}\cdot\boldsymbol{\nabla}\mathbf{B}$ is the material derivative. Note that when the field $\mathbf{B}$ is axisymmetric, the production term $\mathbf{B}\cdot\boldsymbol{\nabla}\mathbf{u}+\boldsymbol{\nabla}\times\left[\alpha(\mathbf{B}\cdot\mathbf{e}_\theta)\mathbf{e}_\theta\right]$ takes the form in cylindrical coordinates

$$\begin{aligned}&\mathbf{B}\cdot\boldsymbol{\nabla}\mathbf{u}+\boldsymbol{\nabla}\times[\alpha(\mathbf{B}\cdot\mathbf{e}_\theta)\mathbf{e}_\theta]\\&\quad=\begin{cases}(B_r\partial_r+B_z\partial_z)u_r-\partial_z(\alpha B_\theta),\\[2pt]\left[B_r(\partial_r-r^{-1})+B_z\partial_z\right]u_\theta,\\[2pt](B_r\partial_r+B_z\partial_z)u_z+r^{-1}\partial_r(r\alpha B_\theta),\end{cases}\end{aligned}\tag{2.6}$$

which clearly shows that the α effect couples the poloidal components of $\mathbf{B}$ to its toroidal component, and the differential rotation couples the poloidal components to the toroidal one (this is the so-called Ω effect).

To avoid ambiguities, in the rest of the paper we call $\mathbf{H}$ the magnetic field and $\mathbf{B}:=\mu\mathbf{H}$ the magnetic induction. The mean-field equation (2.4) is supplemented with the so-called *pseudovacuum* boundary condition $\mathbf{H}\times\mathbf{n}=\mathbf{0}$ at the walls of the vessel, which corresponds to assuming that the exterior of the computational domain is a perfect ferromagnetic material. Preliminary computations (not reported here) done with either the vacuum or the pseudovacuum boundary conditions have shown that the impact of the boundary conditions on the growth rates is not significant when the magnetic permeability of the impeller disks is large (see also [9,16,17]). We henceforth restrict ourselves to the pseudovacuum condition since the computations with this boundary condition use less resources than with the vacuum condition.

The resulting system of partial differential equations is solved using two independent codes, SFEMANS and FV/BEM, presented in [9]. The continuity of the normal component of the magnetic induction $\mathbf{B}$ and that of tangential component of the magnetic field $\mathbf{H}$ are ensured in SFEMANS by using an interior penalty method at the various interfaces. The jump conditions across material interfaces are enforced in FV/BEM by applying simple and robust averaging rules which amount to smoothing the discontinuities.

Since it is reported in [3] that the critical magnetic Reynolds number of the VKS dynamo with soft iron impellers is about 32, we henceforth fix $R_{\rm m}=30$. In the remainder of the paper, we numerically determine the values of the two phenomenological parameters α and μ_b that are critical for dynamo action.

III. THE EXPULSION MECHANISM AND CHOICE OF *h*

Before going through the kinematic dynamo program, we show how the flow parameter h introduced in (2.1) is chosen. Recall that $2h$ is the vertical extension of the column of liquid sodium that is free to move about in the inner cylinder. Our investigation of the influence of the parameter h has been motivated by negative results obtained by other teams and ourselves when assuming that the MND region extends up to $h=0.9$, i.e., includes the blade region. Some of these results, all obtained with $h=0.9$, can be summarized as follows.

(i) Axisymmetric dynamo action occurs for unrealistic values of α (of the order of the maximum velocity of the impellers) when assuming that the distribution of α is localized in the domain swept by the blades and when using either steel impellers ($\mu_d=\mu_b=1$) or perfect ferromagnetic impellers ($\mu_d=\mu_b=\infty$) (see [16,18,19]).

(ii) Axisymmetric dynamo action takes place for realistic values of α (typically a few percent of the maximum velocity) when assuming that the distribution of the α effect is uniform in the entire inner cylinder ($0 \leqslant r \leqslant 1$, $|z| \leqslant 1.3$) and when using soft iron impellers ($\mu_d = \mu_b = 40$ for $0.7 \leqslant |z| \leqslant 1$). However, assuming that α is nonzero in the disks is clearly unphysical [20].

(iii) No dynamo has been obtained using soft iron impellers ($\mu_d = \mu_b = 60$ for $0.7 \leqslant |z| \leqslant 1$) with realistic values of α and distributions of α that all vanish in the impellers. We have tested a uniform distribution in the bulk of the flow and various distributions localized near the impellers without success (results not reported).

These negative results (all obtained with $h = 0.9$) seem to be paradoxical when compared to those from [18] and those from [21] where Ohmic decay tests with various values of R_m and $\alpha = 0$ show that the dominant decaying axisymmetric mode is purely toroidal and localized in the high-permeability domain composing the disks.

In the spirit of [21], we conduct induction tests with $\alpha = 0$ to better evaluate the effect of the high permeability of the two counter-rotating regions and the effect of h. Starting from zero initial data, the test consists of generating an axisymmetric poloidal field by enforcing a current in a closed toroidal loop located in the equatorial plane and of major radius 0.5 and minor radius 0.05. The test is done once with $h = 0.9$ and once with $h = 0.7$. We set $\alpha = 0$, $R_\mathrm{m} = 30$, $\mu_d = 60$, $\mu_b = 10$, and the velocity is the MND field. Note that since $\alpha = 0$ and axisymmetry is assumed, the poloidal magnetic field is not coupled to the toroidal one and dynamo action is not possible [see (2.6)].

Figure 3 shows the time evolution of the magnetic energy, $\frac{1}{2}\int_{\mathcal{D}} \mathbf{B}\cdot\mathbf{H}\,\mathrm{d}v$, in the computational domain $\mathcal{D}$. The results for $h = 0.9$ and $h = 0.7$ are shown in panels (a) and (b), respectively. In both cases the poloidal energy grows first and saturates in about one diffusion time ($t \approx 30 = R_\mathrm{m}$). As expected, the differential rotation within the MND flow produces toroidal magnetic energy through the so-called Ω effect. After about three rotation periods ($t \approx 20$) the toroidal energy becomes larger than the poloidal one and accumulates in the high-permeability domain, i.e., the disk and the blades. Saturation is reached in about 15 rotation periods and the toroidal energy is about three times larger than the poloidal one. Other tests, not reported here, show the same behavior when μ_b varies between 1 and 60.

It is remarkable that the toroidal energy in the case $h = 0.7$ saturates at a level that is 50% higher than when $h = 0.9$. The origin of this difference becomes apparent when inspecting the profiles of the components of the magnetic induction along the vertical line $r = 0.3$, $0 \leqslant |z| \leqslant 1.3$, as shown in Fig. 4. The amplitude of the poloidal components, B_r, B_z, are comparable in the two cases, whereas the amplitude of the toroidal component, B_θ, is significantly larger when $h = 0.7$ than when $h = 0.9$. The ratio $B_\theta(h = 0.7)/B_\theta(h = 0.9)$ is 3 in the soft iron disks ($0.9 \leqslant |z| \leqslant 1$) and 10 in the domain swept by the blades ($0.7 \leqslant |z| \leqslant 0.9$).

Note that the two tangent components of the magnetic induction are discontinuous across the three interfaces $|z| = 0.7$, $|z| = 0.9$, and $|z| = 1$, where the permeability is discontinuous, since the tangential components of the magnetic field $\mathbf{H}\times\mathbf{n}$ are continuous across these interfaces. These jumps are visible on the B_θ component and one should have $(B_\theta^+ - B_\theta^-)/B_\theta^+ = (\mu^+ - \mu^-)/\mu^+$. For instance, for $h = 0.7$, we have $B_\theta(1^+) = 0.0079$, $B_\theta(1^-) = 0.485$, which gives $(B_\theta^+ - B_\theta^-)/B_\theta^+ = -60.4 \approx -59.0 = (\mu^+ - \mu^-)/\mu^+$, then $B_\theta(0.9^+) = 0.486$, $B_\theta(0.9^-) = 0.079$, which gives $(B_\theta^+ - B_\theta^-)/B_\theta^+ = 0.837 \approx 0.833 = (\mu^+ - \mu^-)/\mu^+$, and finally $B_\theta(z = 0.7^+) = 0.061$, $B_\theta(0.7^-) = 0.0056$, which gives $(B_\theta^+ - B_\theta^-)/B_\theta^+ = 0.908 \approx 0.900 = (\mu^+ - \mu^-)/\mu^+$. In conclusion, we observe that the jump conditions are satisfied, although enforced weakly in SFEMANS.

Upon noticing that the radial speed is maximal at $|z| = h$, the above numerical experiment leads us to draw an important conclusion. When $h = 0.9$, the radial component of the MND velocity field, which is large in the volume occupied by the blades $0.7 \leqslant |z| \leqslant 0.9$, sweeps away the toroidal component of the magnetic induction, thereby making the term αB_θ in (2.4) inefficient. In other words, the expulsion effect that occurs when $h = 0.9$ inhibits the action of the α effect in the region where the toroidal magnetic field could be stored. Although the heuristic argument leading to the α effect postulates the existence of swirling jets flowing outward between the blades (see discussion in Sec. II) and in the absence of experimental data, giving us a better knowledge of the flow between the

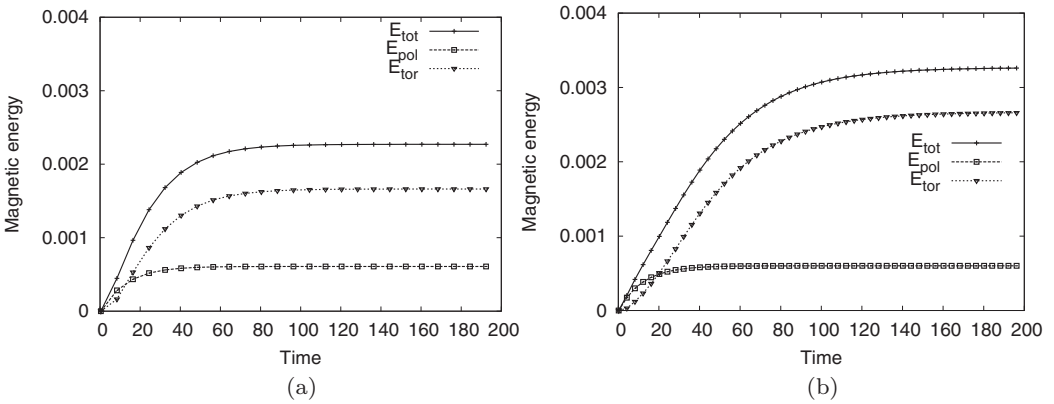

FIG. 3. Time evolution of the toroidal, poloidal, and total magnetic energy in induction runs with the MND velocity field with $\mu_d = 60$, $\mu_b = 10$ using $h = 0.9$ (a) and $h = 0.7$ (b).

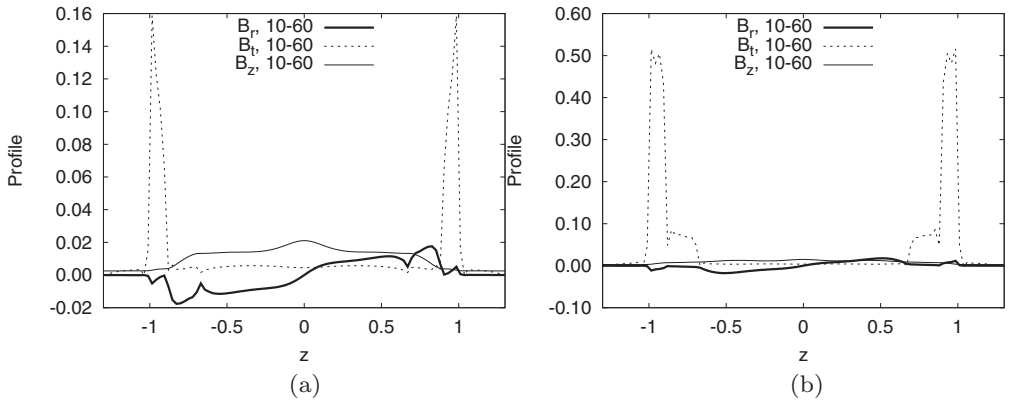

FIG. 4. Induction runs with different MND flows. Profiles as a function of z at $r = 0.3$ of the steady magnetic field with different MND flows: (a) $h = 0.9$; (b) $h = 0.7$.

blades, we choose in the rest of the paper to work with $h = 0.7$. According to (2.2), this choice implies that the radial component of the velocity in the impeller domain (blades and disks) is zero.

IV. DYNAMO ACTION

In this section we look for dynamo action by exploring various scenarios involving μ_d, μ_b, R_m, α, and the MND velocity field. Except in Sec. IV C, we always use the MND velocity field as defined in (2.1)–(2.3). Except in Sec. IV E, all the computations are done assuming axisymmetry of the eigenmodes.

A. Growth rates for $\mu_d = 60$

In the kinematic dynamo framework, the temporal behavior of the magnetic induction can be expressed as $\mathbf{B} = \sum_{n\in\mathbb{N}} \mathbf{B}_n(r,\theta,z)e^{\delta_n t}$, where $(\delta_n, \mathbf{B}_n(r,\theta,z))_{n\in\mathbb{N}}$ are eigenpairs of the differential operator in the right-hand side of (2.4). We henceforth refer to $\gamma := \mathrm{Re}(\delta)$ as the growth rate and $f := \mathrm{Im}(\delta)$ as the frequency; the index n is dropped when the context is unambiguous.

When the angular velocities of the two impellers are exactly opposite (i.e., exact counter-rotation), the geometric configuration possesses the symmetry of rotation by π about any axis contained in the equatorial plane. This symmetry, which we denote R_π (see, e.g., [22, Sec. II C]), is equivalent to the combined action of reflections in $\theta = 0$ and in $z = 0$; more precisely,

$$R_\pi(A_r, A_\theta, A_z)(r,\theta,z) = (A_r, -A_\theta, -A_z)^{\mathsf{T}}(r, -\theta, -z). \tag{4.1}$$

The set of axisymmetric eigenvectors can be classified into two families depending on their invariance by the R_π symmetry. We call dipolar modes the axisymmetric vector fields $\mathbf{B}^D$ such that $R_\pi(\mathbf{B}^D) = -\mathbf{B}^D$, and we call quadrupolar modes the axisymmetric vector fields $\mathbf{B}^Q$ such that $R_\pi(\mathbf{B}^Q) = \mathbf{B}^Q$. These two families of modes are independent and are associated with two distinct families of eigenspaces.

In the rest of this section we use $R_m = 30$, $\mu_b = 10$, and for the permeability of the disks we set $\mu_d = 60$, which is a value close to that measured in [15]. The eigenpairs are computed by using either ARPACK (for SFEMANS) or time integration (for FV/BEM). Table I shows growth rates computed with SFEMANS and FV/BEM for $\alpha \in [-0.03, +0.05]$. For each value of α, the growth rate reported in the table is the largest that is associated with a dipolar eigenmode. Some deviations between the results are evident, which may be caused by slight differences in the space discretization used in each code (e.g., the permeability jumps at the fluid-disk/blade interface are smoothed in FV/BEM) or the way the eigenvalues are evaluated (ARPACK vs time integration).

Figure 5 shows the largest growth rate of the axisymmetric modes with dipolar symmetry (red curve) and with quadrupolar symmetry (blue curve) for $\alpha \in [-0.03, 0.05]$. Dynamo action occurs for $\alpha \leqslant \alpha_c \approx -0.025$ and no dynamo is obtained for positive values of α. The bifurcation happening at α_c is of Hopf type; for instance, for $\alpha = -0.03$, the growth rate is ~ 0.014 and the oscillation period is $T = 2\pi/f = 2\pi/0.072 \approx 87$. We consider that the value of the threshold, $\alpha_c \approx -0.025$, is realistic since the maximal speed of the MND velocity field is one in our advective units. Moreover, that α_c is negative agrees with the heuristic argumentation developed in Sec. II.

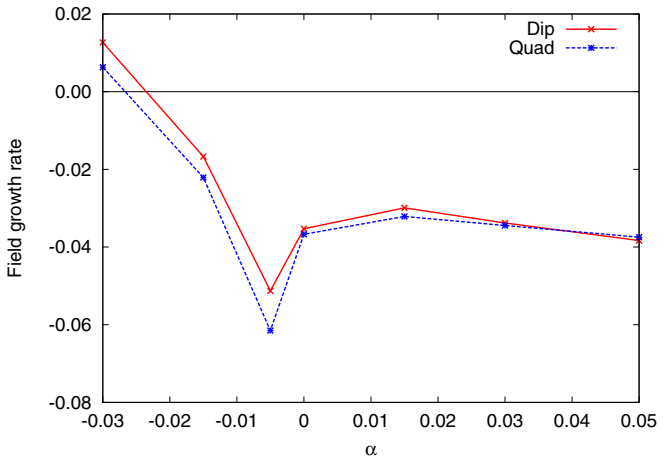

FIG. 5. (Color online) Largest growth rates of axisymmetric modes for $\alpha \in [-0.03, 0.05]$, $R_m = 30$, $\mu_b = 10$, and $\mu_d = 60$ (dipolar and quadrupolar eigenvectors).

The spatial structure of the dipolar eigenmode is shown in Fig. 7(b). The left panel shows the out-of-plane component of the magnetic field and the arrows materializing the poloidal component. The right panel shows the isosurface of 20% of the maximum of the magnetic energy and the magnetic field lines colored by H_z.

B. Comparison with VKS experiment and $\mu_d \to \infty$ limit

The magnetic fields generated in the VKS experiment are mainly axisymmetric, have the dipolar symmetry, and are stationary when close to the threshold and when the two counter-rotating impellers have exactly opposite angular velocities. If the impellers rotate at slightly different frequencies, the magnetic fields that are generated are still axisymmetric, but they are also time dependent and alternate between dipolar and quadrupolar symmetry. The nonoscillating behavior observed when the angular velocities of the two impellers are exactly opposite is also predicted in the low dimensional model of [23] in which the magnetic field is assumed to be the superimposition of a dipolar and a quadrupolar mode. Denoting by D and Q the amplitude of the dipolar and quadrupolar modes, respectively, and assuming that these two modes are coupled through a complex amplitude equation for $A = D + iQ$, it is shown in [23] that the R_π symmetry implies that the normal form for A only admits real coefficients and, under appropriate simplifications, the bifurcation is of pitchfork type. We then face the question of why is it that we find numerically an oscillatory dipolar mode, whereas the dipolar mode in the experiment and in the simplified normal form analysis of [23] is stationary?

One possible answer to this problem is that we are running linear kinematic dynamo simulations and linearity makes the normal form analysis irrelevant. In other words, the dipolar and quadupolar modes that we observe *a priori* live in different eigenspaces and cannot interact. A more satisfactory answer consists of exploring the full range of the parameter μ_d and in particular the limit $\mu_d \to +\infty$. Actually, keeping $\mu_b = 10$, simulations not reported here show that the period of the critical dipolar eigenmode increases as the permeability of the disk μ_d increases and eventually tends to infinity when μ_d goes to $+\infty$. Even more revealing, when setting $\mu_d = +\infty$, the growth rates of the dipole and quadrupole converge to the same values as the α effect becomes stronger as shown in Fig. 6. Actually, the two growth rates coincide when α is less than $\alpha_c \approx -0.012$. This means that the axisymmetric dipolar and quadrupolar eigenmodes coexist in the same eigenspace and are stationary when $\mu_d = +\infty$ (keeping $\mu_b = 10$). It is therefore reasonable to imagine that nonlinearities together with slight imperfections in the experiment (angular velocities not exactly opposite, $\mu_d \neq \infty$) authorize the simultaneous presence of the dipolar and quadrupolar modes, and that the observed magnetic field may oscillate between these two states.

The above conclusion is reinforced when we compare the structure of the eigenmode obtained for $\alpha = -0.03$, $\mu_b = 10$, and $\mu_d = +\infty$ [shown in Fig. 7(a)], with the magnetic field measured at saturation in the VKS experiment (see Fig. 6(b) in [24]). To better evaluate the influence of μ_d, we also show in panel (b) of Fig. 7 the eigenmode obtained with $\mu_d = 60$,

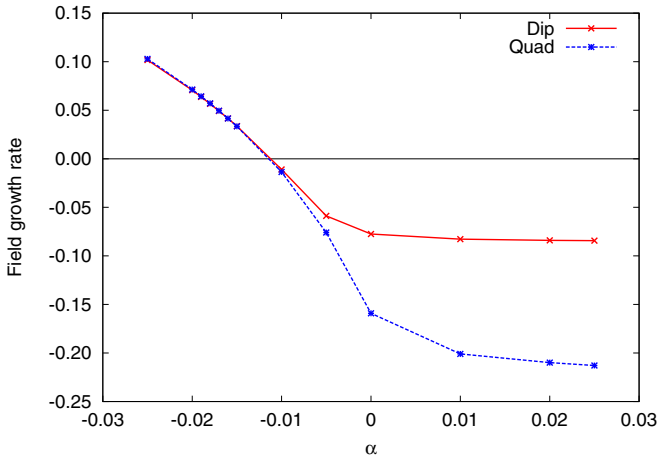

FIG. 6. (Color online) Largest growth rates of axisymmetric modes for $\alpha \in [-0.03, 0.03]$ $R_m = 30$, $\mu_b = 10$, and $\mu_d = \infty$ (dipolar and quadrupolar eigenvectors).

all the other parameters being unchanged. In both Figs. 7(a) and 7(b), the left panel shows the poloidal vector field (H_r, H_z) and the contours of the out-of-plane component of **H**. The out-of-plane magnetic field has extrema close to the impellers and the poloidal field has a very strong axial component close to the rotation axis.

The similarities between the computed and experimental fields are even more striking when we compare the radial profiles of the components of the magnetic field **H** along the lines $z = 0$, $z = \pm 0.51$, as shown on Fig. 8, with those of the magnetic induction **B** in the VKS dynamo at $z = 0$, $z = \pm 0.52$ (see Fig. 5(b) of [24]). Note that $\mathbf{B} = \mu_0 \mathbf{H}$ along the line $z = 0$, $z = \pm 0.52$, which are in the fluid region, where $\mu_r = 1$.

In conclusion, notwithstanding the simplifications made in the present numerical model, the limit $\mu_d \to +\infty$ reproduces very well the observations from both the VKS experiment and the normal form analysis.

C. Role of the poloidal velocity field

In this section we assess the role of the poloidal component of the velocity field by removing its contribution from the MND profile; that is to say, we set $u_r = u_z = 0$ in (2.1) and keep (2.2) and (2.3) unchanged. We also take $\epsilon = 1$ in (2.1)–(2.3) so that the maximum velocity is still equal to 1 in the bulk of the flow. Observe from (2.6) that the generation of the poloidal field (B_r, B_z) now relies only on the α effect; the generation of the toroidal component B_θ through the radial and axial gradients of u_θ is unchanged (Ω effect).

The numerical simulations are done with $\mu_d = 60$, $\mu_b = 10$, and $R_m = 30$. The growth rate of the dipolar mode is shown in panel (a) of Fig. 9; see solid line labeled Dip-noPol. It is remarkable that the capacity of this severely truncated velocity field to produce dynamo action is similar to that of the full MND profile; see line labeled Dip. The spatial distribution of the magnetic field, **H**, obtained with $\alpha = -0.03$ is shown in panel (b) of Fig. 9. Although the growth rate of this mode is very close to that obtained with the full MND profile, the two fields show major differences. The poloidal field and the

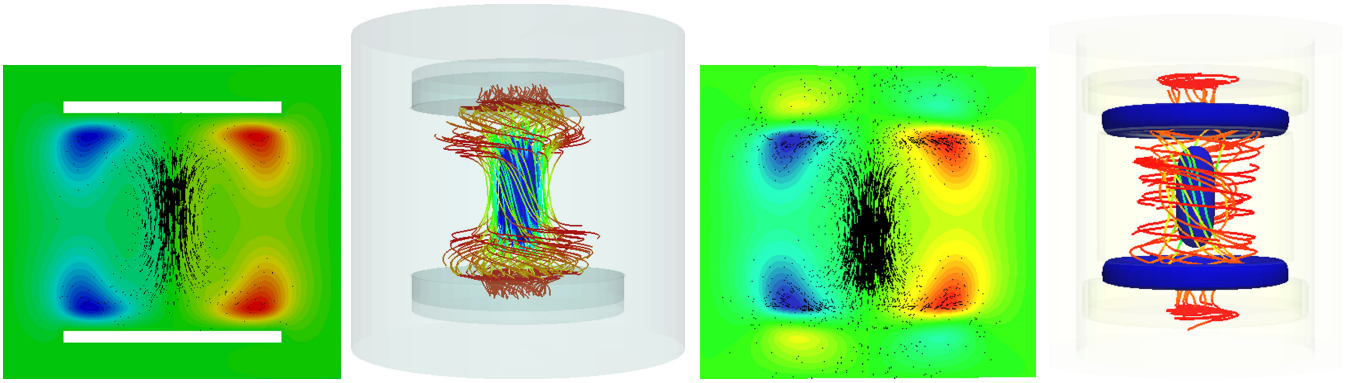

(a) (b)

FIG. 7. (Color online) Dipolar eigenmode for $\mu_d = \infty$ (a) and $\mu_d = 60$ (b), with $\mu_b = 10$, $R_\mathrm{m} = 30$, and $\alpha = -0.03$ in both cases. Shown in panels (a) and (b) are (left) a meridional section, where colors represent the out-of-plane magnetic field component and the arrows materialize the poloidal magnetic field; and (right) an isosurface of 20% of the maximum of the magnetic energy and magnetic field lines colored by H_z [from blue (near axis) $H_z = -0.01$ to red (outside axis) $H_z = 0$].

contours of the out-of-plane magnetic field reveal that the magnetic field is localized close to the impellers.

The radial profiles of the magnetic fields obtained with the truncated and with the full MND velocity field also differ notably, as can be seen in Fig. 10. These simulations show the impact of the poloidal component of the velocity field on the transport of the magnetic field.

D. Influence of μ_b

We now explore the influence of the effective permeability in the region swept by the blades by setting $\mu_b = 60$ and by computing the growth rate of the dipolar mode for $\alpha \in [-0.02, +0.02]$, keeping $\mu_d = 60$ and $R_\mathrm{m} = 30$ and using the full MND field. The results are reported in Fig. 11 and are compared with those already obtained with $\mu_b = 10$. The results shown in the figure have been obtained with SFEMANS, but those given by FV/BEM are similar; for instance, SFEMANS gives $\gamma = 0.158$ and FV/BEM gives $\gamma = 0.167$ for $\alpha = -0.02$. A striking feature of the case $\mu_b = 60$ is that dynamo action is obtained with both positive and negative values of α, as already found in [20], where it is assumed that α is uniformly distributed in the entire computational domain. The bifurcations at $\alpha_c^- \approx -0.0047$ and $\alpha_c^+ \approx +0.0052$ are

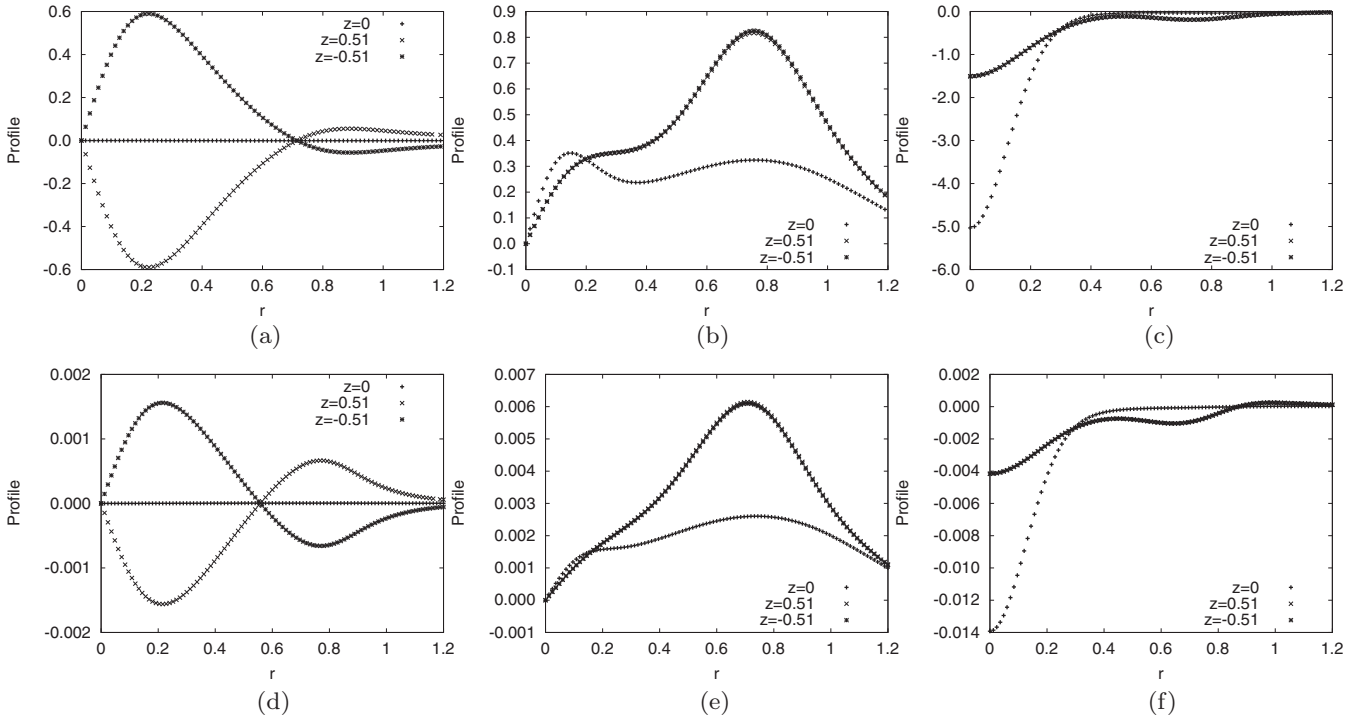

FIG. 8. Dipolar eigenmode for $\mu_d = \infty$ (top row) and $\mu_d = 60$ (bottom row), with $\mu_b = 10$, $R_\mathrm{m} = 30$, and $\alpha = -0.03$. Radial profiles of H_r (a),(d), H_θ (b),(e), and H_z (c),(f) at $z = 0, \pm 0.51$, as indicated.

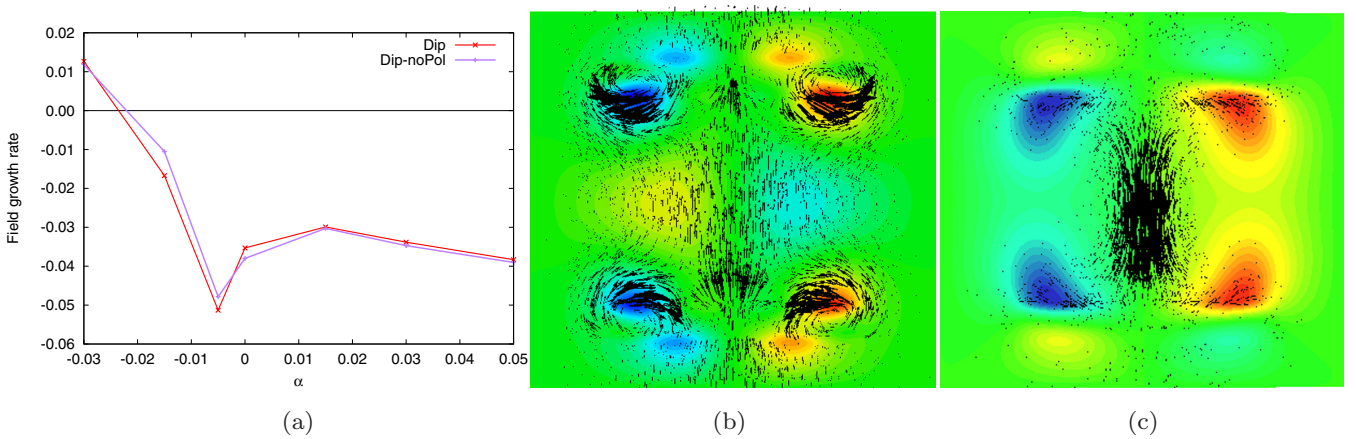

FIG. 9. (Color online) Dynamo runs with the toroidal MND flow using $\mu_b = 10$, $\mu_d = 60$, $R_m = 30$. (a) Comparison of dipolar growth rate versus α for the toroidal MND field (labeled Dip-noPol) and the full MND velocity field (labeled Dip as in Fig. 5). (b) Dipolar eigenmode for $\alpha = -0.03$ using toroidal MND field; (c) Dipolar eigenmode for $\alpha = -0.03$ using full MND field [as in Fig. 7(b)]. Colors represent the out-of-plane component of the magnetic field and the arrows materialize the poloidal component.

both oscillatory. Note that the critical values of α for $\mu_b = 10$ and $\mu_b = 60$ are in proportion of the magnetic permeabilities, i.e., $0.025/0.0047 \approx 5.3 \approx 60/10$, suggesting that the α effect in the blade region is controlled by the product $\alpha\mu_b$.

E. Dynamo with steel material?

Following the VKS experimental results described in [4], we now perform computations with $\alpha = -0.03$ using materials of low magnetic permeability for the blades and the disks. More precisely, we compute the growth rates by making R_m vary in the range [30,430] and by using iron disks and steel blades in one case, and by using disks and blades made of steel in the other case. The first case ($\mu_d = 60$, $\mu_b = 1$) is referred to as run Q in [4], and the second case ($\mu_d = 1$, $\mu_b = 1$) is referred to as run P. The computations are done with SFEMANS using ARPACK, and in each case we look for the leading eigenvalue of the first two azimuthal Fourier modes, which we denote $m = 0$ (axisymmetric mode) and $m = 1$, respectively. The results are reported in panel (a) of Fig. 12 for run Q and in panel (b) for run P.

An axisymmetric dynamo is obtained for $R_m \geqslant R_m^c \approx 120$ for the composite impellers, i.e., run Q. The first unstable mode is quadrupolar. The Fourier mode $m = 1$ has a negative growth rate in the range $0 \leqslant R_m \leqslant 130$ and has the structure of a stationary equatorial dipole. The threshold $R_m^c \approx 120$ for axisymmetric dynamo action is compatible with the threshold ~ 190 estimated in [4] for run Q by extrapolating measured decay rates at various magnetic Reynolds numbers. No dynamo action is obtained for $R_m \leqslant 430$ when the impellers are made of steel, i.e., run P. This conclusion is again in agreement with that from [4]. These numerical experiments show that it is necessary to have blades made of a material with a relative magnetic permeability larger than 1 to obtain dynamo action in the VKS experiment at a magnetic Reynolds number less than 70, which is the upper bound that can be reached with the current power supply.

V. CONCLUDING REMARKS

The kinematic dynamo simulations presented in this paper are based on a mean-field model relying on three phenomenological parameters: the magnetic permeability of the disks, μ_d; the effective permeability of the domain swept by the blades, μ_b; the component $\mathbb{a}_{\theta\theta}$ of the α tensor. For the α-effect model to be effective with realistic values of α, i.e., a few percent of the reference velocity scale, it is necessary to have a large value of μ_d. For the critical magnetic Reynolds number to be within the limits of the power supply available in the VKS

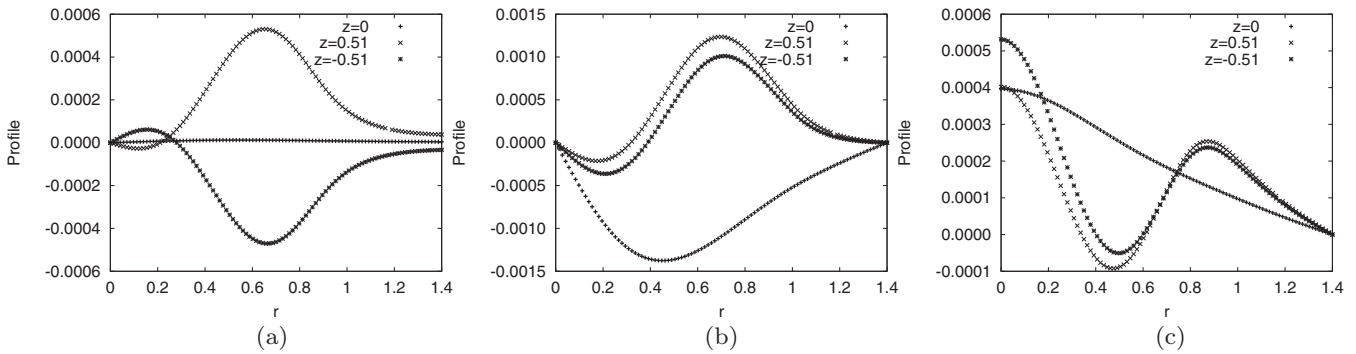

FIG. 10. Dynamo runs with the toroidal MND velocity field for $\mu_b = 10$, $\mu_d = 60$, $R_m = 30$, and $\alpha = -0.03$. Radial profiles of H_r (a), H_θ (b), and H_z (c) at $z = 0, \pm 0.51$ as indicated.

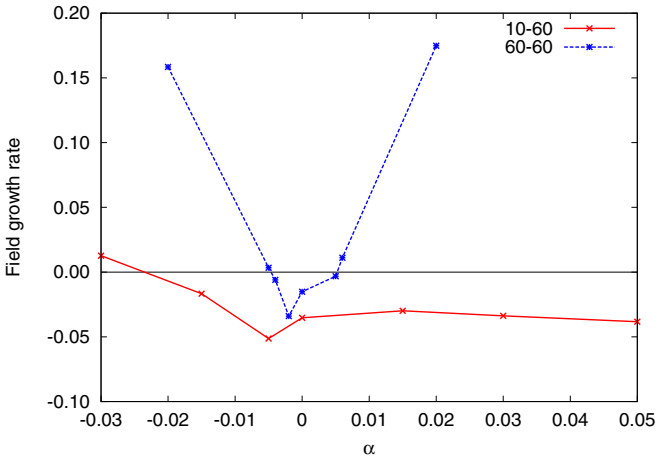

FIG. 11. (Color online) Largest growth rate of the axisymmetric dipolar mode with $\mu_d = 60$ for $\alpha \in [-0.03, 0.05]$, using either $\mu_b = 10$ (as in Fig. 5, solid line labeled 10-60) or $\mu_b = 60$ (dashed line labeled 60-60).

experiment, it is also necessary that the blades be made of a material of moderately large permeability.

A. Similarities with the VKS dynamo

The model exhibits features that are all observed in the VKS experiment.

(i) Dynamo action occurs at $R_m = 30$ using a realistic value of α (say, $\alpha = -0.03$) when the disks are composed of soft iron and the effective permeability in the region swept by the blades is large enough ($\mu_b = 10$).

(ii) The two most unstable modes at $R_m = 30$ are axisymmetric and have dipolar and quadrupolar symmetry, respectively. These modes are slowly oscillatory and occur at different thresholds on α when $\mu_d = 60$, but they become steady and the corresponding two eigenspaces merge to form a two-dimensional vector space when $\mu_d \to +\infty$. These two modes are observed to exist in the VKS experiment when the rotation frequencies of the two impellers are different.

(iii) The most unstable mode at $R_m = 30$ is an axisymmetric dipole when the angular velocities of the two impellers are exactly opposite. This mode is dominated by the B_z component close to the axis and by the B_θ component in the vicinity of the impellers (see Fig. 7). The spatial distribution of this mode is very close to that observed at saturation in the VKS experiment (see Fig. 6(b) of [24]). The radial profiles of the components of the magnetic field along the lines $z = 0$, $z = \pm 0.51$ are also close to those observed experimentally (compare Figs. 8 and 5(b) of [24]).

(iv) Dynamo action is possible with soft iron disks and steel blades using a realistic value of α (say $\alpha = -0.03$), but the corresponding critical magnetic Reynolds number is close to 120, making it unobservable with the power supply that is currently available in the VKS experiment. The most unstable mode is an axisymmetric quadrupole. Induction experiments reported in [4] suggest that the critical R_m could be ~ 190, which is roughly in agreement with our estimate considering that our definition of R_m is different from that in [4] [see discussion before (2.4)].

(v) No dynamo action occurs with steel impellers (both the disks and the blades made of steel) with a realistic value of α (say $\alpha = -0.03$) in the range $R_m \in [30,430]$. We have also verified (results not shown here) that there is no dynamo action at $R_m = 30$ in the range $\alpha \in [-5, +5]$. Moreover, induction experiments reported in [4] suggest that turbulence dissipation increases with R_m, which suggests that dynamo action may not be possible in any reasonable range for the magnetic Reynolds number with steel impellers.

B. Tentative scenario for the VKS dynamo

Our model agrees with the induction experiments reported in [4] and confirms that the presence of ferromagnetic material is important to understand the VKS experiment. The numerical simulations reported in the present paper and those reported in [9,21] then lead us to think that the interaction between the ferromagnetic material and the recirculating flow between the blades may be a potential candidate for the source of the VKS

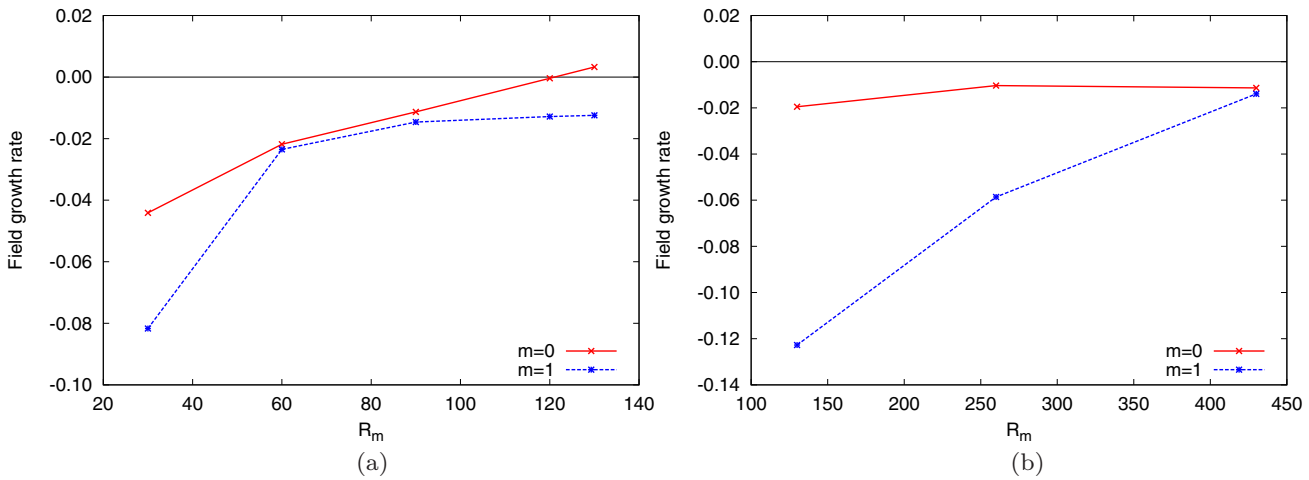

FIG. 12. (Color online) Growth rates of Fourier modes $m = 0$ (solid line labeled $m = 0$) and $m = 1$ (dashed line labeled $m = 1$) with $\alpha = -0.03$ for $R_m \in [30,430]$: (a) with $\mu_b = 1$, $\mu_d = 60$; (b) with $\mu_b = 1$, $\mu_d = 1$.

dynamo. More precisely, we propose the following three step scenario:

(1) accumulation of toroidal energy in the disks when μ_d is large;

(2) creation of poloidal energy in the blade region by interaction between the toroidal mean field that accumulates in the disks and the velocity field recirculating between the blades;

(3) transport by the bulk flow throughout the entire vessel and generation of toroidal energy by Ω effect.

The accumulation of toroidal energy in the disks is supported by previous studies reported in [9,21]. It is shown therein that the disks have a strong tendency to store toroidal energy as μ_d grows (see Figs. 5 and 6 in [21] and Figs. 5 and 7 in [9]). Moreover, the linear stability analysis (without α modeling) shows that the axisymmetric mode (though decaying) is dominant when $\mu_d \geqslant 18$ (see Fig. 5 in [21]). The recirculating velocity field between the blades interacts with the axisymmetric toroidal mean field that dominates in the neighborhood of the disks. The small scale radial perturbations of the magnetic field are focalized and amplified by the blades when μ_b is large, as shown in [25]; this is the localized α effect (see Fig. 2).

This tentative scenario is reminiscent of the flux transport dynamo mechanism frequently invoked for the solar dynamo. Recall that this model of the solar cycle is based on the accumulation of toroidal energy in the tachocline region (transition region between the solar convective and radiative zones), the production of poloidal energy due to the α effect induced by the helicity generated by simultaneous action of buoyancy and Coriolis acceleration, and finally a meridional transport by the bulk flow between the equator and the poles. Contrary to the conventional picture of a dynamo loop where poloidal and toroidal energies are locally coupled, in flux transport models the coupling occurs sequentially in separate regions.

The above model is still speculative and its validation would require a better knowledge of the fluid flow between the blades, which is a difficult task, either experimentally or numerically, even in the purely hydrodynamical case: Flow measurements between the blades are just starting [26] and the lack of resolution is a permanent challenge for direct numerical simulations. Finally, let us recall that further nonlinear MHD computations aiming at realistically reproducing the VKS dynamo will have to overcome the challenge of having to deal with very small magnetic Prandl numbers ($R_m/R_e \ll 1$), and to account for blades made of soft iron they will have to properly implement jump conditions on moving boundaries.

ACKNOWLEDGMENTS

The authors want to thank Wietze Herreman for stimulating discussions. A.G. acknowledges support from the Helmholtz Alliance LIMTECH. The HPC resources for SFEMaNS were provided by GENCI-IDRIS (Grant No. 2013-0254) in France. J.-L.G. acknowledges support from University Paris Sud 11 and National Science Foundation Grant No. NSF DMS-1015984.

[1] A. Gailitis, O. Lielausis, S. Dement'ev, E. Platacis, and A. Cifersons, Detection of a flow induced magnetic field eigenmode in the Riga dynamo facility, Phys. Rev. Lett. **84**, 4365 (2000).

[2] R. Stieglitz and U. Müller, Experimental demonstration of a homogeneous two-scale dynamo, Phys. Fluids **13**, 561 (2001).

[3] R. Monchaux, M. Berhanu, M. Bourgoin, Ph. Odier, M. Moulin, J.-F. Pinton, R. Volk, S. Fauve, N. Mordant, F. Pétrélis, A. Chiffaudel, F. Daviaud, B. Dubrulle, C. Gasquet, L. Marié, and F. Ravelet, Generation of magnetic field by a turbulent flow of liquid sodium, Phys. Rev. Lett. **98**, 044502 (2007).

[4] S. Miralles, N. Bonnefoy, M. Bourgoin, Ph. Odier, J.-F. Pinton, N. Plihon, G. Verhille, J. Boisson, F. Daviaud, and B. Dubrulle, Dynamo threshold detection in the von Kármán sodium experiment, Phys. Rev. E **88**, 013002 (2013).

[5] S. Kreuzahler, D. Schulz, H. Homann, Y. Ponty, and R. Grauer, Numerical study of impellerdriven von Kármán flows via a volume penalization method, New J. Phys. **16**, 103001 (2014).

[6] R. Monchaux, M. Berhanu, S. Aumaitre, A. Chiffaudel, F. Daviaud, B. Dubrulle, F. Ravelet, S. Fauve, N. Mordant, F. Pétrélis, M. Bourgoin, Ph. Odier, J.-F. Pinton, N. Plihon, and R. Volk, The von Kármán sodium experiment: Turbulent dynamical dynamos, Phys. Fluids **21**, 035108 (2009).

[7] L. Marié, C. Normand, and F. Daviaud, Galerkin analysis of kinematic dynamos in the von Kármán geometry, Phys. Fluids **18**, 017102 (2006).

[8] F. Ravelet, A. Chiffaudel, F. Daviaud, and J. Léorat, Towards an experimental von Kármán dynamo: numerical studies for an optimized design, Phys. Fluids **17**, 117104 (2005).

[9] A. Giesecke, C. Nore, F. Stefani, G. Gerbeth, J. Léorat, F. Luddens, and J.-L. Guermond, Electromagnetic induction in non-uniform domains, Geophys. Astrophys. Fluid Dyn. **104**, 505 (2010).

[10] F. Krause and K.-H. Radler, *Mean-Field Magnetohydrodynamics and Dynamo Theory* (Pergamon Press, Oxford, U.K., 1980).

[11] K.-H. Rädler, *Encyclopedia of Geomagnetism and Paleomagnetism* (Springer, Netherlands, 2007), pp. 192–199.

[12] F. Pétrélis, N. Mordant, and S. Fauve, On the magnetic fields generated by experimental dynamos, Geophys. Astrophys. Fluid Dyn. **101**, 289 (2007).

[13] F. Ravelet, B. Dubrulle, F. Daviaud, and P.-A. Ratié, Kinematic alpha tensors and dynamo mechanisms in a von Kármán swirling flow, Phys. Rev. Lett. **109**, 024503 (2012).

[14] R. Stepanov, R. Volk, S. Denisov, P. Frick, V. Noskov, and J.-F. Pinton, Induction, helicity and alpha effect in a toroidal screw flow of liquid gallium, Phys. Rev. E **73**, 046310 (2006).

[15] G. Verhille, N. Plihon, M. Bourgoin, Ph. Odier, and J.-F. Pinton, Induction in a von Kármán flow driven by ferromagnetic impellers, New J. Phys. **12**, 033006 (2010).

[16] R. Laguerre, C. Nore, A. Ribeiro, J. Léorat, J.-L. Guermond, and F. Plunian, Impact of impellers on the axisymmetric magnetic mode in the VKS2 dynamo experiment, Phys. Rev. Lett. **101**, 104501 (2008).

[17] C. Gissinger, A. Iskakov, S. Fauve, and E. Dormy, Effect of magnetic boundary conditions on the dynamo threshold of von Kármán swirling flows, Europhys. Lett. **82**, 29001 (2008).

[18] A. Giesecke, C. Nore, F. Plunian, R. Laguerre, A. Ribeiro, F. Stefani, G. Gerbeth, J. Léorat, and J.-L. Guermond, Generation of axisymmetric modes in cylindrical kinematic mean-field dynamos of VKS type, Geophys. Astrophys. Fluid Dyn. **104**, 249 (2010).

[19] R. Laguerre, C. Nore, A. Ribeiro, J. Léorat, J.-L. Guermond, and F. Plunian, Erratum: Impact of impellers on the axisymmetric magnetic mode in the VKS2 dynamo experiment [Phys. Rev. Lett. 101, 104501 (2008)], Phys. Rev. Lett. **101**, 219902(E) (2008).

[20] A. Giesecke, F. Stefani, and G. Gerbeth, Role of soft-iron impellers on the mode selection in the von Kármán–sodium dynamo experiment, Phys. Rev. Lett. **104**, 044503 (2010).

[21] A. Giesecke, C. Nore, F. Stefani, G. Gerbeth, J. Léorat, W. Herreman, F. Luddens, and J.-L. Guermond, Influence of high-permeability discs in an axisymmetric model of the Cadarache dynamo experiment, New J. Phys. **14**, 053005 (2012).

[22] C. Nore, L. S. Tuckerman, O. Daube, and S. Xin, The 1[ratio]2 mode interaction in exactly counter-rotating von Kármán swirling flow, J. Fluid Mech. **477**, 51 (2003).

[23] F. Pétrélis and S. Fauve, Chaotic dynamics of the magnetic field generated by dynamo action in a turbulent flow, J. Phys.: Condens. Matter **20**, 494203 (2008).

[24] J. Boisson, S. Aumaitre, N. Bonnefoy, M. Bourgoin, F. Daviaud, B. Dubrulle, Ph. Odier, J.-F. Pinton, N. Plihon, and G. Verhille, Symmetry and couplings in stationary von Kármán sodium dynamos, New J. Phys. **14**, 013044 (2012).

[25] H. Zaidi, C. Nore, A. Bossavit, F. Bouillault, and J.-L. Guermond, Whitney element approach for dynamo action modeling with a von Kármán type velocity, in IEEE Transaction on Magnetics, Sixth Biennal IEEE Conference on Electromagnetic Field Computation, Annecy, France, 2014 (to be published).

[26] J. Burguete (private communication).